PHYSICAL SCIENCE


10.1126/sciadv.1601318

# Nanogeochronology of discordant zircon measured by atom probe microscopy of Pb-enriched dislocation loops

**Emily M. Peterman,[1]* Steven M. Reddy,[2,3] David W. Saxey,[2,4] David R. Snoeyenbos,[5] William D. A. Rickard,[2,4] Denis Fougerouse,[2,3] Andrew R. C. Kylander-Clark[6]**

**Isotopic discordance is a common feature in zircon that can lead to an erroneous age determination, and it is attributed to the mobilization and escape of radiogenic Pb during its post-crystallization geological evolution. The degree of isotopic discordance measured at analytical scales of ~10 µm often differs among adjacent analysis locations, indicating heterogeneous distributions of Pb at shorter length scales. We use atom probe microscopy to establish the nature of these sites and the mechanisms by which they form. We show that the nanoscale distribution of Pb in a ~2.1 billion year old discordant zircon that was metamorphosed c. 150 million years ago is defined by two distinct Pb reservoirs. Despite overall Pb loss during peak metamorphic conditions, the atom probe data indicate that a component of radiogenic Pb was trapped in 10-nm dislocation loops that formed during the annealing of radiation damage associated with the metamorphic event. A second Pb component, found outside the dislocation loops, represents homogeneous accumulation of radiogenic Pb in the zircon matrix after metamorphism. The $^{207}Pb/^{206}Pb$ ratios measured from eight dislocation loops are equivalent within uncertainty and yield an age consistent with the original crystallization age of the zircon, as determined by laser ablation spot analysis. Our results provide a specific mechanism for the trapping and retention of radiogenic Pb during metamorphism and confirm that isotopic discordance in this zircon is characterized by discrete nanoscale reservoirs of Pb that record different isotopic compositions and yield age data consistent with distinct geological events. These data may provide a framework for interpreting discordance in zircon as the heterogeneous distribution of discrete radiogenic Pb populations, each yielding geologically meaningful ages.**

## INTRODUCTION

Zircon is a commonly dated mineral because it can be chemically and physically robust, it incorporates U during growth, and yet it excludes Pb (the daughter product of U decay) during crystallization. The difference in decay rates between $^{238}U$ and $^{235}U$ provides a mechanism to assess concordance of calculated radiometric ages. Although the diffusivity of Pb in non-metamict zircon is negligible under most geologic conditions (*1*), discordance in the U-Pb system is common (*2*–*4*). Most discordant dates are younger than the initial zircon crystallization event because Pb is lost from the crystal in response to discrete geologic events or via diffusion over longer time scales during high-temperature metamorphic events. Lead is more easily lost from zircon in which the lattice has been affected by radiation damage from α-recoil (*5*–*7*), by crystal-plastic deformation that produces fast-diffusion pathways (*8*), or by low-temperature hydrothermal dissolution-reprecipitation reactions (*9*, *10*). For radiation-damaged zircon, metamorphism can initially increase Pb diffusivity at rates that outpace crystal annealing, thus resulting in Pb loss and discordant U/Pb dates (*11*). Despite Pb loss, discordant zircon analyses may provide useful chronological information; upper intercepts potentially indicate the crystallization age and lower intercepts commonly reflect a specific younger geologic event, such as metamorphism (*2*, *11*), meteorite impact events (*12*, *13*), or the timing of deformation (*14*).

The degree of isotopic discordance may differ among spot analyses collected from a single zircon. For example, laser ablation inductively coupled plasma mass spectrometry (LA-ICP-MS) and secondary ion mass spectrometry (SIMS) data indicate that adjacent 10- to 25-µm-diameter spots can be up to 65% different in isotopic discordance (*15*). Heterogeneous distribution of Pb below the scale of SIMS and LA-ICP-MS analysis can explain these differences. However, the controls on small-scale Pb retention in zircon, and their effect on isotopic discordance and geological interpretation, remain largely unknown. Small amounts of Pb may be incorporated into the lattice as $Pb^{2+}$ [or $Pb^{4+}$; see discussion in Kramers *et al.* (*16*) and Kogawa *et al.* (*17*)], but previous studies of zircon have suggested that radiogenic Pb is likely retained in sites that minimize elastic strain, such as crystal defects (*18*), metallic nanospheres (*19*), and metamict domains (*20*). Despite documenting Pb migration at the nanometer (*18*) and micrometer scales (*20*, *21*), these previous studies report only concordant or reversely discordant SIMS ages from these domains and have not recognized discordance associated with Pb loss.

This study focuses on a well-characterized, normally discordant zircon grain located in the matrix of a garnet-kyanite metapelite (sample 57082, zircon 26) collected near Xanthi in the Central Greek Rhodope. Following regional nomenclature (*22*), the Rhodope Metamorphic Complex is divided into four main tectonic units that were juxtaposed during the Paleogene: the Lower, Middle, Upper, and Uppermost

[1]Earth and Oceanographic Science, Bowdoin College, Brunswick, ME 04011, USA. [2]Geoscience Atom Probe Facility, Advanced Resource Characterisation Facility, John de Laeter Centre, Curtin University, GPO Box U1987, Perth, Western Australia 6845, Australia. [3]Department of Applied Geology, Western Australian School of Mines, Curtin University, GPO Box U1987, Perth, Western Australia 6845, Australia. [4]Department of Physics and Astronomy, Curtin University, GPO Box U1987, Perth, Western Australia 6845, Australia. [5]Department of Geosciences, University of Massachusetts, Amherst, MA 01003, USA. [6]Department of Earth Science, University of California, Santa Barbara, Santa Barbara, CA 93106, USA.
*Corresponding author: Email: epeterma@bowdoin.edu

Allochthons. The metapelite from this study is located at the base of the Middle Allochthon, adjacent to the Nestos Shear Zone. The Middle Allochthon was thrust southwest over the Lower Allochthon during Alpine convergence (*22*, *23*) and is composed of continental- and oceanic-derived lithologies along with orthogneisses derived from Late Jurassic to Early Cretaceous intrusions. Zircon geochronology from garnet-kyanite metapelites at Xanthi indicates a detrital population characterized by crystallization intervals at 475 to 520 million years ago (Ma), 560 to 670 Ma, 1.8 to 1.9 billion years ago (Ga), and 2.0 to 2.1 Ga (*23*, *24*). Zircon dates from 560 to 670 Ma and 2.0 to 2.1 Ga have previously been interpreted as recycled Gondwanan crust (*24*, *25*). The maximum deposition age of the metapelite is 417 Ma, based on the youngest concordant detrital zircon core (*23*).

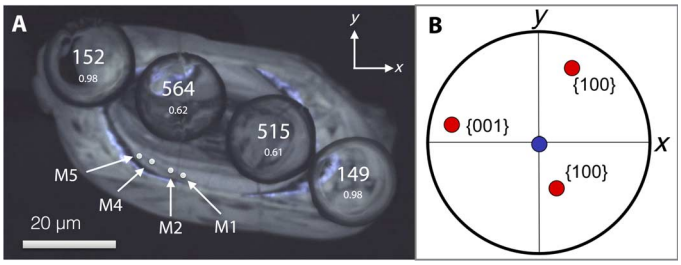


**Fig. 1. Cathodoluminescence (CL) image, analysis spots, and EBSD orientation map.** (**A**) CL image of analyzed zircon showing oscillatory zoning in the core. Arrows labeled with an "M" point to atom probe analysis locations; large spots mark laser ablation split stream (LASS) analysis locations; $^{206}Pb/^{238}U$ dates are shown in white; the concordance of each spot analysis is reported below each date. Uncertainty is conservatively estimated at 2%. (**B**) Pole figure showing the orientation data for the analyzed zircon grain. Red dots show the orientation of major crystallographic planes constrained by EBSD. The blue dot shows the orientation of atom probe specimen tips.

Metamorphic diamond in the metapelites at the Xanthi (*23*, *26*) and Sidironero (*27*) localities of the Middle Allochthon indicates metamorphism at ultrahigh-pressure (UHP) conditions (>4.5 GPa, c. 800°C), but no diamond was found in the analyzed sample. The timing of UHP metamorphism in the Middle Allochthon remains controversial. At Xanthi, monazite U-Th-Pb electron microprobe dates suggest UHP metamorphism at c. 186 Ma (*28*). Some studies interpret UHP metamorphism as a single, protracted event that began at this time (*23*), whereas other studies suggest multiple UHP and HP events from Jurassic to Eocene time (*22*, *24*, *29*). Additional constraints on the timing of metamorphism are provided by zircon rims from garnet-kyanite metapelites near Xanthi; these rims yield $^{206}Pb/^{238}U$ dates that record granulite to upper amphibolite facies metamorphism after UHP conditions at c. 149 to 144 Ma (*23*, *24*, *30*). This metamorphic event has been interpreted as either a second HP event (*27*, *30*, *31*) or plastic deformation and thermal re-equilibration during protracted exhumation (*23*). Zircon U/Pb dates <65 Ma are consistent with activity along the Nestos Shear Zone (*23*).

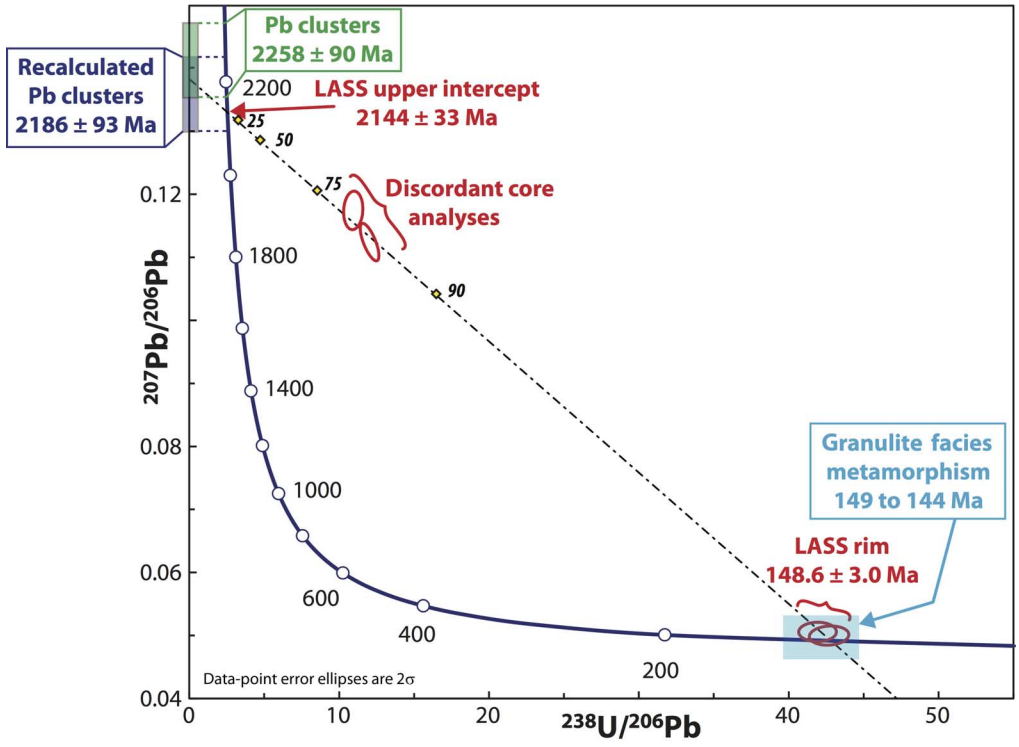


**Fig. 2. Tera-Wasserburg plot of zircon dates from LASS and APM data.** Ellipses show results from LASS core and rim analyses with 2σ uncertainty. The discordia line (dashed) constructed from the LASS data indicates an upper intercept of 2144 ± 33 Ma with a lower intercept of 148.6 ± 3.0 Ma. The lower intercept agrees with the timing of clustering of Pb in the zircon core (Fig. 3). The light blue field marks the range of published U-Pb dates measured from zircon rims formed at this time (*23*, *30*). The $^{207}Pb/^{206}Pb$ dates were calculated from the atom probe data (boxes with 1σ uncertainty); dashed lines project onto concordia. The green box is the $^{207}Pb/^{206}Pb$ date from all clusters; the dark blue box is the $^{207}Pb/^{206}Pb$ date corrected for encapsulation at 160 Ma. Yellow diamonds show the modeled effect of Pb loss (%) on U-Pb dates for a zircon that crystallized at 2.15 Ga and was metamorphosed at 150 Ma; italicized numbers correspond to % Pb loss.

## RESULTS

### Scanning electron microscopy

The core of the zircon grain analyzed in this study exhibits oscillatory zoning observed in cathodoluminescence (CL). The core-rim boundary is marked by a thin, CL-dark envelope and a CL-bright domain (shown as pale blue in RainbowCL; Fig. 1A) located on the rim side of the boundary. Electron backscatter diffraction (EBSD) analysis reveals a crystalline grain with no intragrain misorientations and similar band contrast values for the core and rim domains; the [001] direction of the zircon is oriented 20° from the polished surface (Fig. 1B).

### LASS-ICP-MS

LASS-ICP-MS analyses were acquired using a spot size that measures 15 μm in diameter and up to 8 μm in depth, which represents a sampling volume of c. $1.4 \times 10^3$ $\mu m^3$. LASS analysis of the core yields $^{206}Pb/^{238}U$ dates of 564 ± 24 and 515 ± 18 Ma (2σ). These dates are 38 and 39 % discordant, as measured by the ratio of the $^{206}Pb/^{238}U$ and $^{207}Pb/^{235}U$ dates (analytical results are provided in table S1). The rim yields concordant $^{206}Pb/^{238}U$ dates of 149 ± 2 and 152 ± 2 Ma (2σ uncertainty; Fig. 2). U and Th concentrations measured from the core and rim domains differ considerably. The core contains c. 1050 parts per million (ppm) U and 120 ppm Th, whereas the rim contains c. 450 ppm U and 3 ppm Th (full analytical results are provided in table S1). It is possible that some of the discordance observed in the LASS core analyses may be attributed to mixing between core and rim domains. However, the marked contrast in U and Th concentrations in these domains would require the mixed LASS analysis to be >90% from the rim; the CL image of the grain after LASS (Fig. 1A) indicates that this is not likely. Geochemical analyses of the discordant core (see table S1) show a positive Ce anomaly, a negative Eu anomaly, and a steep chondrite-normalized heavy rare earth element (HREE) profile (see fig. S1); these data are consistent with magmatic growth in the presence of plagioclase (*32*). The rims exhibit relatively flat chondrite-normalized HREE profiles, a positive Ce anomaly, and a weakly negative Eu anomaly, which are consistent with equilibration with garnet during metamorphism (*32*, *33*). A discordia line pinned by the metamorphic rim through the discordant core analyses indicates an upper intercept of 2144 ± 33 Ma [Fig. 2; calculated using Isoplot 4.15 (*34*)].

### Atom probe microscopy

Four atom probe specimens ("tips") were analyzed from the core of the zircon (Fig. 1A); each tip yielded 37 to 41 million atoms, which represents a sample volume of c. $1.7 \times 10^{-3}$ $\mu m^3$ for the sum of the atom probe tips. A representative atom probe mass spectrum is shown in Fig. 3; atom probe acquisition and reconstruction parameters are provided in tables S2 and S3. In all four tips, we observe homogeneous distributions of the principal zircon components Zr, Si, O, and Hf. Uranium is measured at concentrations between 60 and 120 parts per million atoms (ppma). A peak-to-background ratio of 0.1 to 0.25 limits the detection of inhomogeneities in U (see fig. S2), but it appears homogeneous for variations above 100 ppma and scale lengths greater than 10 nm. The tip (M1) that sampled a CL-dark zone within the core has more U than the other tips (see table S4). Lead is predominantly found as atom clusters measuring up to 10 nm in diameter (Fig. 4); within the clusters, signal-to-noise ratio is sufficiently high enough to identify $^{206}Pb$ and $^{207}Pb$ (see Fig. 3, inset). The number of clusters differs among the atom probe tips; only one Pb cluster was found within

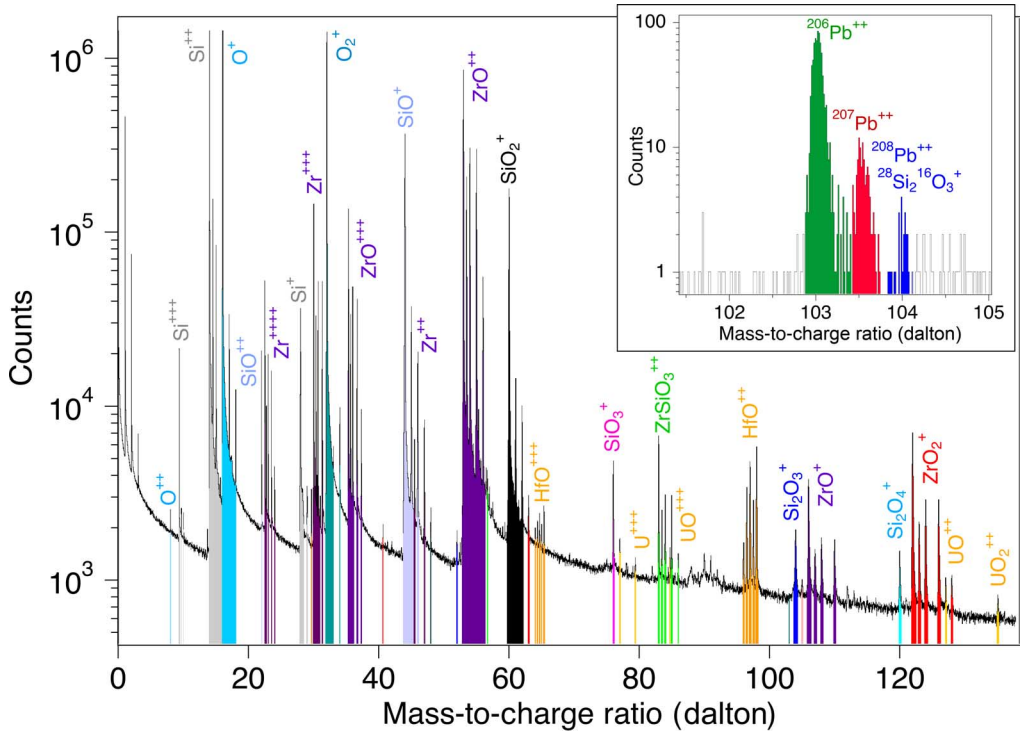


**Fig. 3. APM mass spectrum.** Representative atom probe microscopy (APM) mass spectrum acquired from tip M1. Peaks are color-coded by molecular species and/or element. Inset: Mass spectrum for atoms local to cluster IV (Fig. 4) showing distinct mass peaks for $^{206}Pb$ and $^{207}Pb$. $^{208}Pb$ (if present) coincides with a $Si_2O_3$ molecular species and cannot be quantified.

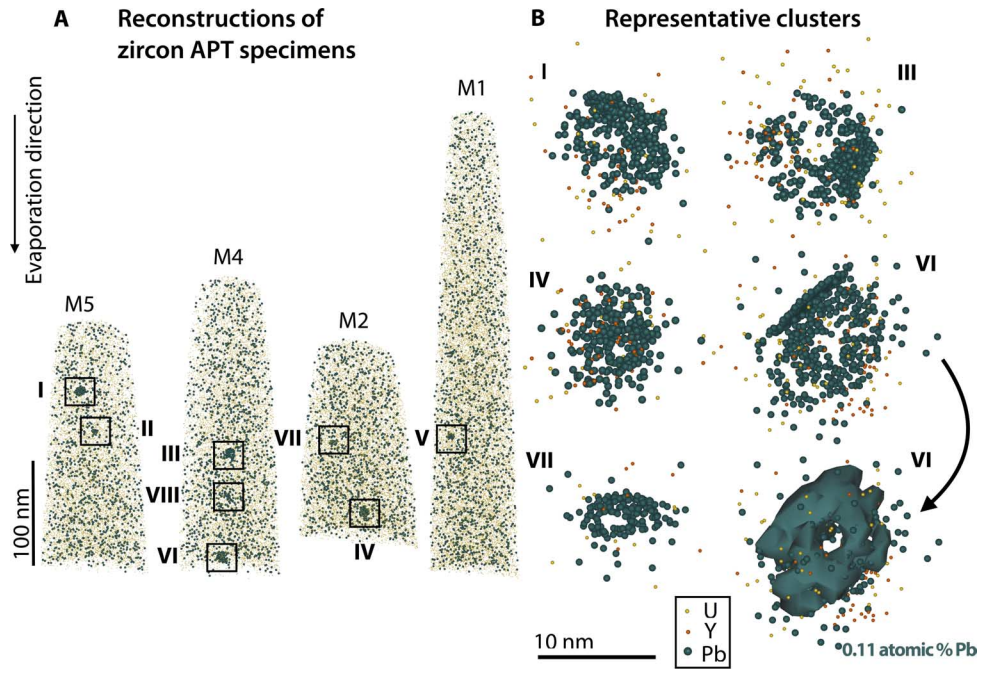


**Fig. 4. APM reconstructions from the discordant 2.1-Ga zircon.** (**A** and **B**) Reconstructed tips showing clustered distributions of Pb (green) atoms without co-clustering of U (yellow) atoms (A). Each tip measures between 200 and 500 nm in length. Roman numerals correspond to clusters shown in (B) and table S2. All tips are shown at the same scale; arrangement follows the sequence across the zircon shown in Fig. 1A. Rotating 3D projections are included in videos S1 to S4. (B) Individual Pb atoms (large green spheres) in clusters are shown with U (yellow) and Y (orange) atoms. All clusters are shown at the same scale. Cluster VI is also shown with an isoconcentration surface defined at 0.11 atomic % Pb to illustrate the toroidal morphology.

**Table 1. Atom probe data from Pb clusters.** Tip refers to the specimen number (see Figs. 1 and 3). Roman numerals correspond to clusters shown in Fig. 3. Pb counts are the number of background-corrected $^{206}$Pb and $^{207}$Pb atoms counted per cluster. Background-corrected $^{207}$Pb/$^{206}$Pb ratios are reported with 1σ uncertainty. $^{207}$Pb/$^{206}$Pb dates for each cluster are reported with 1σ uncertainty. The sum of the clusters is labeled "Total."

| Tip | Cluster | Pb counts (atoms) | | Corrected $^{207}$Pb/$^{206}$Pb ratio ±1σ | Date (Ma) ±1σ |
|---|---|---|---|---|---|
| | | $^{206}$Pb | $^{207}$Pb | | |
| M5 | I | 564 | 84 | 0.149 ± 0.019 | 2334 ± 210 |
| | II | 176 | 24 | 0.134 ± 0.033 | 2151 ± 443 |
| M4 | VIII | 93 | 15 | 0.160 ± 0.053 | 2456 ± 590 |
| | VI | 900 | 142 | 0.157 ± 0.015 | 2424 ± 163 |
| | III | 786 | 107 | 0.136 ± 0.016 | 2177 ± 221 |
| M2 | IV | 824 | 108 | 0.131 ± 0.015 | 2111 ± 202 |
| | VII | 126 | 17 | 0.134 ± 0.038 | 2151 ± 515 |
| M1 | V | 87 | 11 | 0.123 ± 0.046 | 2000 ± 713 |
| **Total** | | **3556** | **507** | **0.142 ± 0.0074** | **2258 ± 90** |

tip M1, which measures c. 400 nm in length, whereas several clusters were found in M4 and are located <50 nm apart. Rotating three-dimensional (3D) reconstructions of the tips are available as videos S1 to S4. Some clusters (for example, cluster VI; Fig. 4B) appear asymmetrical with Pb enrichment at the "top" of some clusters; this enrichment reflects preferential evaporation of Pb relative to other atoms as the evaporation surface propagated into a Pb-enriched cluster (see Materials and Methods). Despite this analytical artefact, we observe that the distribution of Pb in the cluster defines a toroidal morphology (Fig. 4B). The clusters differ in both the number of Pb atoms (c. 90 to 1000 atoms) and the Pb concentration (2.0 to 5.5 atomic %); some are associated with enrichment in Y and Al (up to 1 atomic %; see table S2). No other REEs or U were detected within the clusters above the local detection limit (approximately 500 ppma). This limit corresponds to a maximum U enrichment of four to eight times.

The $^{207}$Pb/$^{206}$Pb ratios of all clusters are within uncertainty of each other and yield values of 0.1233 to 0.1598 (Table 1). Summing the background-corrected counts of Pb atoms from the clusters, the $^{207}$Pb/$^{206}$Pb ratio calculated from the clusters corresponds to a $^{207}$Pb/$^{206}$Pb date of 2258 ± 90 Ma (Table 1 and Fig. 2).

## DISCUSSION

### Geologic evolution preserved in zircon

Since crystallization, the zircon has undergone exhumation, erosion and transportation, and sedimentary redeposition. The timing of these

processes is poorly constrained, but the zircon rims indicate metamorphism at 150 Ma (Fig. 2), a result consistent with previous geochronological studies (*23*, *30*) of this locality. We interpret that the ~150-Ma metamorphic rims formed during granulite facies metamorphism and that prograde metamorphism associated with this event produced Pb loss, which resulted in a discordant core. The upper intercept calculated from the LASS-ICP-MS data is 2144 ± 33 Ma (Fig. 2), which is interpreted as the original crystallization age (Fig. 4) and is consistent with ages of other detrital zircons from this locality (*24*). To evaluate the magnitude of Pb loss, we used the crystallization age (determined from the upper intercept) and calculated expected isotopic ratios assuming the grain was concordant. Comparison of these ratios with measured ratios indicate >75% Pb loss for both core analyses [calculated after Wetherill (*4*); yellow diamonds in Fig. 2 illustrate isotopic ratios for modeled % Pb loss].

The calculated $^{207}Pb/^{206}Pb$ date from the sum of Pb atoms detected within the clusters (2258 ± 90 Ma) overlaps this crystallization age (2144 ± 33 Ma), but because there is no detectable U within the cluster, it is unlikely that the $^{207}Pb/^{206}Pb$ ratio evolved significantly after encapsulation within the clusters. Therefore, the $^{207}Pb/^{206}Pb$ ratio from the clusters can be recalculated to reflect the separation of parent and daughter isotopes during the prograde path of the metamorphic event dated by the rims at 150 Ma. Although not directly constrained by these data, a reasonable timing estimate for the initiation of prograde metamorphism associated with the 150 Ma granulite-facies event is 160 Ma. The actual timing of prograde metamorphism may predate 160 Ma; thus, this estimate is interpreted as a minimum encapsulation time. Correcting the $^{207}Pb/^{206}Pb$ date measured from the clusters for the timing of Pb encapsulation at 160 Ma yields a date of 2186 ± 93 Ma (Fig. 2, blue box). This date provides a better match with the original crystallization age determined by the upper intercept from the LASS data (Fig. 2) and, thus, provides further support for the encapsulation of Pb during prograde metamorphism.

In the zircon matrix outside the clusters, the Pb isotopic ratio continued to evolve (Fig. 5). Although additional $^{206}Pb$ accumulated from the decay of $^{238}U$ after metamorphism, very little $^{207}Pb$ accumulated after 150 Ma because of the low concentration of $^{235}U$ on Earth at this time. Hence, the much larger LASS analysis volume (c. $1.4 \times 10^3$ μm$^3$ versus $1.7 \times 10^{-3}$ μm$^3$) represents mixing of two distinct reservoirs within the core: a higher $^{207}Pb/^{206}Pb$ component in the clusters and a lower $^{207}Pb/^{206}Pb$ in the matrix (Fig. 5). Because of the heterogeneous distribution of Pb-enriched clusters, different proportions of these reservoirs as sampled by the LASS volume can thus yield different amounts of discordance.

## Trapping radiogenic Pb

These data provide some constraints on the sites and mechanisms by which Pb may become trapped during overall Pb-loss events. In the analyzed grain, Pb mobility was likely enhanced by radiation damage, which is known to significantly increase the diffusivity of Pb over that in undamaged zircon (*35*). The calculated dose of ~$8.7 \times 10^{15}$ decay events/mg from this zircon (c. 1050 ppm U and c. 120 ppm Th; 2 Ga) is above the first percolation point ($2 \times 10^{15}$ decay events/mg) for zircon, which suggests that the zircon should be metamict, unless it has been annealed. However, the zircon in this study is highly crystalline, as indicated by similar band contrast values from both core and rim domains as measured by EBSD (*36*, *37*). Therefore, this zircon was likely annealed close to the metamorphic temperature peak, which would repair much of the radiation damage, thereby inhibiting Pb loss by diffusion. We interpret that most Pb loss occurred as temperatures increased during the prograde path of the Late Jurassic granulite facies metamorphic event.

Although some crystal defects, such as screw and edge dislocations, are expected to persist within zircon after annealing, these defects do not explain the toroid-shaped clusters (Fig. 4B). One defect type that has this geometry is a dislocation loop. Dislocation loops have been observed to form in zircon during growth or through annealing of radiation damage resulting from an α-decay radiation dose of >$10^{16}$ decay events/mg (*38*), which compares favorably with the calculated dose (~$8.7 \times 10^{15}$ decay events/mg). Transmission electron microscopy (TEM) studies indicate that these dislocation loops lie in {101} planes in zircon and measure between 10 and 100 nm in diameter (*38*). Although the orientations of the toroids in this study are not well constrained, their dimensions are broadly consistent with the published TEM data (Fig. 4B).

With regard to the size and distribution of observed dislocation loops, studies (*39*–*41*) have shown that annealing preferentially favors large dislocation loops at the expense of small or faulted dislocation loops. Under conditions of vacancy supersaturation while the zircon crystal is annealing radiation damage, large loops continue to grow. Conditions of vacancy undersaturation, reached after annealing radiation damage, favor the contraction of large loops. Therefore, geologic annealing would likely eliminate many of the smallest loops and may also cause contraction of the larger loops, which is consistent with the toroid diameter (c. 10 nm) measured in the atom probe data (Fig. 4B).

It is also notable that the clusters are defined principally by Pb and Al, which can be interstitial in zircon (*17*, *32*, *42*). The clustering of interstitial atoms within dislocation loops is well known in materials science (*43*) and has recently been observed in Ni-coated Si wafers implanted with $As^+$. In these experiments, APM revealed that interstitial Ni atoms migrated to dislocations, and decorated dislocation loops during heat treatment (*44*). The clustering of Ni within dislocation loops produces an energetically favorable state for the material because it reduces elastic strain on the crystal lattice caused by the distributed dislocations and the interstitial atoms. Similar reductions in strain on the crystal lattice would occur in zircon.

Dislocation loops are thus appropriate in scale, distribution, and morphology to explain the clusters observed in the atom probe data, and they also provide a mechanism for trapping radiogenic Pb. As described schematically in Fig. 5, metamorphism likely enhanced Pb diffusion in the zircon core and also promoted annealing; the complex annealing process is ultimately responsible for producing the loops we observe via atom probe. As Pb diffused through radiation-damaged zircon during the prograde phase of the Late Jurassic metamorphic event, Pb atoms were trapped by dislocation loops that were forming as part of the annealing process. Pb atoms not trapped in dislocation loops diffused out of the crystal during the prograde path of the same metamorphic event, thus explaining a mechanism to preserve isotopically meaningful Pb clusters despite the entire grain losing >75% of its radiogenic Pb.

Previous atom probe studies have also focused on Pb reservoirs in zircon. For example, Valley *et al.* (*18*) describe Pb clusters in 4.4-Ga concordant zircon from the Jack Hills, Australia. The $^{207}Pb/^{206}Pb$ ratios from these clusters are consistent with having formed in response to a thermal event that mobilized and accumulated Pb and Y in radiation damage sites produced by α-recoil from the decay of U (and Th). Piazolo *et al.* (*20*) highlight the association of Pb loss along fast-diffusion

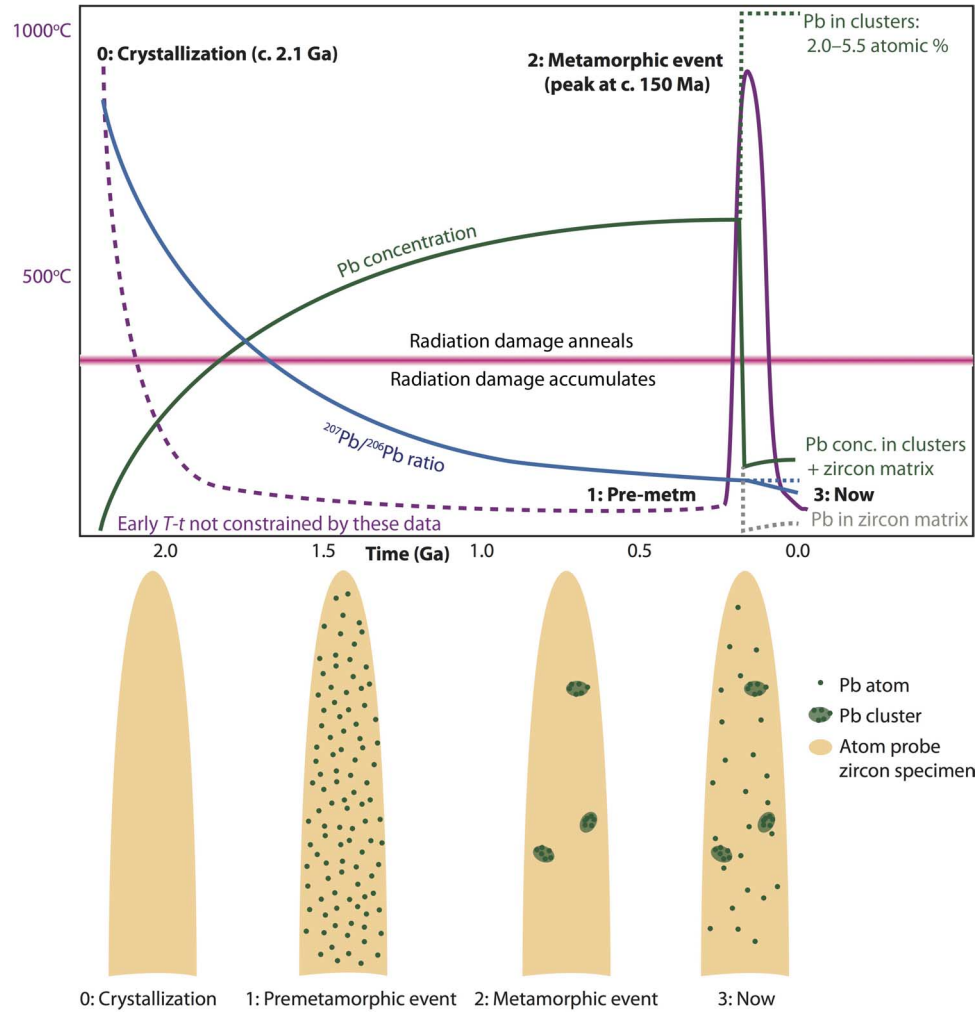


**Fig. 5. Schematic history of the zircon. 0:** Grain crystallized (c. 2.1 Ga). Inferred Pb accumulation in the crystal (green curve) and temperature decrease (purple curve) as the source material was exhumed. **1:** Before metamorphism (Pre-metm), Pb is randomly distributed throughout the specimen. $^{207}Pb/^{206}Pb$ evolves according to U decay constants (blue curve). Radiation damage accumulates below the critical amorphization temperature [magenta bar; 360°C for zircon with 1000 ppm U (*1*, *6*)]. **2:** During the prograde portion of the high-temperature (*T*) metamorphic event at c. 150 Ma, >75% of Pb is lost from the crystal (sharp drop on the solid green curve). The remaining Pb diffuses into dislocation loops, resulting in heterogeneously distributed Pb with high concentrations (2.0 to 5.5 atomic %) within the dislocation loops (dashed green line). **3:** Pb continues to accumulate in the crystal after Pb loss (gray dashed line), thus evolving the bulk ratio within the tip (solid green line). Because the zircon lost Pb, newly accumulated Pb has a larger effect on the $^{207}Pb/^{206}Pb$ ratio of the whole tip (blue curve). The Pb ratio within the clusters does not change significantly (blue dashed line) because there is no detected U within the clusters.

pathways produced by deformation with Pb localization in metamict domains. The Pb clusters presented here differ in two important ways. First, the paucity of clusters amid a relatively homogeneous distribution of U argues against Pb localization in α-recoil damage sites [cf. Valley *et al.* (*18*)] and does not explain the distribution of clusters observed in the four atom probe specimens. Second, the discordance measured from the zircon cores by LASS requires extensive radiogenic Pb loss, indicating differences in both Pb diffusion distances and the mechanism for retaining radiogenic Pb between discordant and concordant zircon. Furthermore, although Pb can collect in metamict domains, the lack of lattice misorientations and the high degree of crystallinity of the zircon analyzed, as inferred from the EBSD collected in this study, suggest that trapping Pb in metamict domains does not fully explain the origin, morphology, and distribution of the Pb clusters.

The presence of Pb-enriched clusters in all four measured specimens, the consistency among the $^{207}Pb/^{206}Pb$ ratios within the clusters, and the associated enrichment in other interstitial elements within these clusters as measured by atom probe have significant implications for geochronology and geochemistry. The data reveal that discordant zircon can contain nanoscale clusters associated with the trapping of radiogenic Pb in dislocation loops. In this example, the formation of dislocation loops and the enhanced Pb mobility are caused by increased temperature associated with metamorphism, such that the loops mark the timing of metamorphism and the isotopically distinct Pb reservoirs

held by the loops preserve evidence of the original crystallization age. This discordant zircon thus comprises a mixture of different concordant populations with different isotopic compositions. Atom probe analysis of discordant zircon thus has the potential to yield geologically meaningful ages from nanoscale domains. Future advances in instrument design to enhance detector efficiency are anticipated to improve the statistics associated with the dates calculated from the Pb-enriched clusters. These data demonstrate that, even in discordant zircon with a high-temperature metamorphic history, geologically meaningful dates can be recovered by atomic-scale isotopic microscopy.

## MATERIALS AND METHODS

### Experimental design

The primary objectives of this study were to document the distribution of U and Pb within discordant zircon, to identify other enrichment patterns, and to calculate isotopic dates from APM data. To accomplish this, four atom probe specimens were prepared from the core of a single zircon grain. Before preparation for the atom probe, the zircon was analyzed via SEM and LASS to provide a petrographic context for the atom probe data.

### Methods

**SEM-CL.** A doubly polished thick section (100 μm) was prepared from a garnet-kyanite schist from Xanthi (see Introduction). To minimize charging, the section was coated with a thin (<10 nm) layer of carbon. Zircon was imaged using a RainbowCL detector and a TESCAN backscattered electron detector on a TESCAN VEGA3 scanning electron microscope operated at 10 kV and 250 pA at Bowdoin College.

**LASS-ICP-MS.** Geochemical and geochronologic data were collected simultaneously via LASS-ICP-MS performed at the University of California, Santa Barbara. Methods largely followed those from Kylander-Clark *et al.* (*45*). Polished sample sections and epoxy-mounted reference materials were loaded in a Photon Machines HelEx cell connected to a 193-nm excimer laser (Photon Machines) at the LASS Facility at the University of California, Santa Barbara. The Nu Plasma multi-collector ICP-MS measured U-Th-Pb isotopes, and the Agilent 7700x quadrupole ICP-MS measured Zr, Si, P, Ti, Y, Nb, Hf, and REE. To remove surface contamination, each spot was pretreated with two laser pulses. The laser was operated at 4 Hz for 20 s. Operating conditions (for example, tuning parameters and gas flows) were optimized for a 15-μm-diameter spot that measures <8 μm in depth.

We used 91500 [1062.4 ± 0.4 Ma (*46*)] and GJ-1 (*47*) as primary reference materials for age and composition, respectively. The piece of GJ-1 used in these is 601.7 ± 1.3 Ma [$^{206}Pb/^{238}U$ date (*45*)]. Plešovice [337.13 ± 0.37 Ma (*48*)] and Peixe [564 ± 4 Ma (*49*)] were also analyzed as secondary reference materials. Plešovice yielded a $^{206}Pb/^{238}U$ date of 334.8 ± 1.8 Ma [mean square of weighted deviates (MSWD) = 0.58, $n$ = 16], Peixe yielded a $^{206}Pb/^{238}U$ date of 573.6 ± 3.4 (MSWD = 0.19; $n$ = 14), and GJ-1 yielded a $^{206}Pb/^{238}U$ date of 606.9 ± 2.3 Ma (MSWD = 0.29, $n$ = 39). These uncertainties represent internal uncertainties only and are not propagated for systematic biases.

Each analytical run began with a block of six analyses on the reference materials. The reference material block was followed by a series of blocks on unknowns (five to eight spots per block) and blocks on reference materials (two spots per block). At the end of the run, a second block of reference material analyses ($n$ = 6) was measured. Ratios were bias-, drift-, and age-corrected using Iolite (*50*) following procedures detailed in Kylander-Clark *et al.* (*45*). Although the uncertainty on an individual ratio is typically <1% (2σ), the long-term reproducibility of secondary reference materials is c. 1.5% (2σ) and is attributed to variation in laser energy and gas flow within the cell (*45*). To account for measurement uncertainty, the assumed uncertainty in the age of 91500, and the long-term reproducibility of the reference materials analyzed, we conservatively assigned 2% uncertainty (2σ) to all unknown analyses.

**SEM-EBSD.** Before EBSD analysis, polished sections were weighted with halved brass rods and polished for 3 hours in a noncrystallizing colloidal silica suspension on a Buehler VibroMet 2 vibratory polisher [SYTON method of Fynn and Powell (*51*)]. To minimize charging, the section was coated with a thin (<5 nm) layer of carbon. EBSD data were acquired using a TESCAN MIRA field emission gun SEM equipped with an Oxford EBSD at Curtin University. The MIRA was operated at 20 kV and 15 nA. EBSD data were collected using an Oxford Nordlys system and optimized at 25 ms per frame, and data were acquired using Oxford Instruments AZtec software and post-processed with Channel 5.12 software.

**Focused ion beam SEM.** Following EBSD analysis, the zircon was prepared for atom probe analysis using a TESCAN LYRA3 focused ion beam SEM at Curtin University. The site-selective sample lift-out and tip-sharpening procedure was adapted from methods described by Thompson *et al.* (*52*). Final atom probe needle tip diameters were <150 nm, and the half-shank angles were 6° to 10°. All tips were oriented normal to the polished crystal face (see Fig. 1). Ga implantation was minimized by a final polishing annulus with a beam energy of 5 kV.

**APM.** Recent advances in APM instrument design now permit isotopic tomography of minerals at the nanometer scale (*18*, *53*–*56*), thus providing an unprecedented view of the 3D elemental and isotopic structure and composition of a specimen. Details of the local electrode atom probe (LEAP) are described elsewhere (*57*); pertinent analytical conditions are reported here.

The Advanced Resource Characterisation Facility's Geoscience Atom Probe laboratory features a Cameca LEAP 4000X HR equipped with a laser pulsing system and a reflectron to enhance isotopic resolution. Within the LEAP, each specimen was cooled to ~60 K under ultrahigh vacuum ($10^{-11}$ torr), with a high voltage applied to facilitate field evaporation of atoms from the tip surface. An ultraviolet (λ = 355 nm) laser was focused on the specimen apex and pulsed at 200 kHz, with an energy of 100 pJ per pulse, to control the ion evaporation process; full acquisition parameters are detailed in table S2. The voltage was gradually increased during the analysis from c. 3 to 10 kV to maintain an ion detection rate of 0.006 to 0.008 ions per pulse. Ions were recorded on a position-sensitive detector, and the composition was determined using time-of-flight mass spectrometry. This enables the 3D reconstruction of the position and composition of atoms within the specimen, with a spatial resolution on the order of 0.3 nm. Each specimen tip yielded approximately $4 \times 10^7$ ions. The mass resolving power for each data set was c. 1000 (full width at half maximum). Data reconstruction and analysis were performed using IVAS (Integrated Visualization & Analysis Software; version 3.6.12) from Cameca Instruments Inc.; reconstruction parameters are provided in table S3. High-resolution SEM images of specimen tips before and after acquisition were used to constrain the spatial reconstruction parameters.

The enrichment in Pb within the clusters results in a sudden evaporation, which can be observed as the near-planar top of the largest Pb

clusters (Fig. 4). From a practical standpoint, uneven evaporation produces an artefact in the reconstruction, wherein the centroid of the trace element distributions (for example, Y and Al) is significantly shifted down the *z* axis with respect to Pb. Therefore, to identify the composition of the atoms spatially associated with the Pb clusters, we first used a Pb isoconcentration surface to select the atoms local to a cluster and then re-ranged the mass spectrum of this subset to eliminate noise and identify new peaks. We then constructed a new isoconcentration surface by combining all trace elements that were enhanced locally to each cluster: Pb, Y, Al, Sc, P, and Ti. We re-ranged the mass spectrum defined by this new composite surface and used it to generate the cluster concentrations. Because of the offset between the Pb and the other trace elements, the data cannot be displayed strictly as a function of distance from the cluster center. Instead, table S4 shows the composition of the "whole" cluster, as defined by the trace element isoconcentration surface for each Pb cluster. These methods are consistent with the general approach proposed by Kelly and Larson (*57*) for reconstructing atom probe data from materials with differing evaporation fields.

## SUPPLEMENTARY MATERIALS

Supplementary material for this article is available at http://advances.sciencemag.org/cgi/content/full/2/9/e1601318/DC1

Supplementary Methods

table S1. Extended data table for LASS-ICP-MS analysis of zircon.

table S2. Acquisition parameters for atom probe analysis on the LEAP 4000X HR at Curtin University.

table S3. Reconstructions were performed with the following parameters using the "voltage evolution" algorithm in IVAS 3.6.12.

table S4. Extended data table from the LEAP analysis (matrix and clusters).

fig. S1. Chondrite-normalized REE plot for the zircon core (green) and rim (black) analyses.

fig. S2. U portion of mass spectrum from tip M1 (analytical run 0654) showing two of the four mass peaks used to quantify the U content.

video S1. This video shows a 360° rotation about the *z* axis of reconstructed atom probe data from M1 (see Fig. 1 for location).

video S2. This video shows a 360° rotation about the *z* axis of reconstructed atom probe data from M2 (see Fig. 1 for location).

video S3. This video shows a 360° rotation about the *z* axis of reconstructed atom probe data from M4 (see Fig. 1 for location).

video S4. This video shows a 360° rotation about the *z* axis of reconstructed atom probe data from M5 (see Fig. 1 for location).

## REFERENCES AND NOTES


1. D. J. Cherniak, E. B. Watson, Pb diffusion in zircon. *Chem. Geol.* **172**, 5–24 (2001).
2. K. Mezger, E. J. Krogstad, Interpretation of discordant U-Pb zircon ages: An evaluation. *J. Metamorph. Geol.* **15**, 127–140 (1997).
3. S. L. Harley, N. M. Kelly, Zircon Tiny but Timely. *Elements* **3**, 13–18 (2007).
4. G. W. Wetherill, Discordant uranium-lead ages, I. *Eos. Trans. AGU* **37**, 320–326 (1956).
5. R. T. Pidgeon, J. R. O'Neil, L. T. Silver, Uranium and lead isotopic Stability in a metamict zircon under experimental hydrothermal conditions. *Science* **154**, 1538–1540 (1966).
6. A. Meldrum, L. A. Boatner, W. J. Weber, R. C. Ewing, Radiation damage in zircon and monazite. *Geochim. Cosmochim. Acta* **62**, 2509–2520 (1998).
7. L. T. Silver, S. Deutsch, Uranium-lead isotopic variations in zircons: A case study. *J. Geol.* **71**, 721–758 (1963).
8. S. M. Reddy, N. E. Timms, P. Trimby, P. D. Kinny, C. Buchan, K. Blake, Crystal-plastic deformation of zircon: A defect in the assumption of chemical robustness. *Geology* **34**, 257–260 (2006).
9. T. Geisler, R. T. Pidgeon, W. van Bronswijk, R. Kurtz, Transport of uranium, thorium, and lead in metamict zircon under low-temperature hydrothermal conditions. *Chem. Geol.* **191**, 141–154 (2002).
10. T. Geisler, U. Schaltegger, F. Tomaschek, Re-equilibration of zircon in aqueous fluids and melts. *Elements* **3**, 43–50 (2007).
11. J. N. Connelly, Degree of preservation of igneous zonation in zircon as a signpost for concordancy in U/Pb geochronology. *Chem. Geol.* **172**, 25–39 (2001).
12. A. Nemchin, N. Timms, R. Pidgeon, T. Geisler, S. Reddy, C. Meyer, Timing of crystallization of the lunar magma ocean constrained by the oldest zircon. *Nat. Geosci.* **2**, 133–136 (2009).
13. A. J. Cavosie, T. M. Erickson, N. E. Timms, S. M. Reddy, C. Talavera, S. D. Montalvo, M. R. Pincus, R. J. Gibbon, D. Moser, A terrestrial perspective on using ex situ shocked zircons to date lunar impacts. *Geology* **43**, 999–1002 (2015).
14. D. E. Moser, W. J. Davis, S. M. Reddy, R. L. Flemming, R. J. Hart, Zircon U–Pb strain chronometry reveals deep impact-triggered flow. *Earth Planet. Sci. Lett.* **277**, 73–79 (2009).
15. L. Nasdala, R. T. Pidgeon, D. Wolf, G. Irmer, Metamictization and U-PB isotopic discordance in single zircons: A combined Raman microprobe and SHRIMP ion probe study. *Miner. Petrol.* **62**, 1–27 (1998).
16. J. Kramers, R. Frei, M. Newville, B. Kober, I. Villa, On the valency state of radiogenic lead in zircon and its consequences. *Chem. Geol.* **261**, 4–11 (2009).
17. M. Kogawa, E. B. Watson, R. C. Ewing, S. Utsunomiya, Lead in zircon at the atomic scale. *Am. Mineral.* **97**, 1094–1102 (2012).
18. J. W. Valley, A. J. Cavosie, T. Ushikubo, D. A. Reinhard, D. F. Lawrence, D. J. Larson, P. H. Clifton, T. F. Kelly, S. A. Wilde, D. E. Moser, M. J. Spicuzza, Hadean age for a post-magma-ocean zircon confirmed by atom-probe tomography. *Nat. Geosci.* **7**, 219–223 (2014).
19. M. A. Kusiak, D. J. Dunkley, M. J. Whitehouse, S. A. Wilde, K. Marquardt, Metallic lead nanospheres discovered in ancient zircons. *Proc. Natl. Acad. Sci. U.S.A.* **112**, 4958–4963 (2015).
20. S. Piazolo, A. La Fontaine, P. Trimby, S. Harley, L. Yang, R. Armstrong, J. M. Cairney, Deformation-induced trace element redistribution in zircon revealed using atom probe tomography. *Nat. Commun.* **7**, 10490 (2016).
21. M. A. Kusiak, M. J. Whitehouse, S. A. Wilde, A. A. Nemchin, C. Clark, Mobilization of radiogenic Pb in zircon revealed by ion imaging: Implications for early Earth geochronology. *Geology* **41**, 291–294 (2013).
22. M. Janák, N. Froitzheim, N. Georgiev, T. J. Nagel, S. Sarov, *P-T* evolution of kyanite eclogite from the Pirin Mountains (SW Bulgaria): Implications for the Rhodope UHP Metamorphic Complex. *J. Metamorph. Geol.* **29**, 317–332 (2011).
23. K. Krenn, C. Bauer, A. Proyer, U. Klötzli, G. Hoinkes, Tectonometamorphic evolution of the Rhodope orogen. *Tectonics* **29**, TC4001 (2010).
24. A. Liati, Identification of repeated Alpine (ultra) high-pressure metamorphic events by U–Pb SHRIMP geochronology and REE geochemistry of zircon: The Rhodope zone of Northern Greece. *Contrib. Mineral. Petrol.* **150**, 608–630 (2005).
25. D. Gebauer, in *Pre-Mesozoic Geology in the Alps*, J. F. v. Raumer, F. Neubauer, Eds. (Springer, Berlin, 1993), pp. 93–117.
26. E. D. Mposkos, D. K. Kostopoulos, Diamond, former coesite and supersilicic garnet in metasedimentary rocks from the Greek Rhodope: A new ultrahigh-pressure metamorphic province established. *Earth Planet. Sci. Lett.* **192**, 497–506 (2001).
27. S. Schmidt, T. J. Nagel, N. Froitzheim, A new occurrence of microdiamond-bearing metamorphic rocks, SW Rhodopes, Greece. *Eur. J. Mineral.* **22**, 189–198 (2010).
28. T. Reischmann, D. Kostopoulos, Timing of UHPM in metasediments from the Rhodope Massif, N Greece. *Geochim. Cosmochim. Acta* **66** (Suppl. 1), 633 (2002).
29. M. Kirchenbaur, J. Pleuger, S. Jahn-Awe, T. J. Nagel, N. Froitzheim, R. O. C. Fonseca, C. Münker, Timing of high-pressure metamorphic events in the Bulgarian Rhodopes from Lu–Hf garnet geochronology. *Contrib. Mineral. Petrol.* **163**, 897–921 (2011).
30. A. Liati, D. Gebauer, C. M. Fanning, *Ultrahigh- Pressure Metamorphism: 25 Years after the Discovery of Coesite and Diamond*, L. Dobrzhinetskaya, S. W. Garyad, S. Wallis, S. Cuthbert, Eds. (Elsevier, London, 2011), pp. 295–324.
31. E. Mposkos, A. Krohe, I. Baziotis, Alpine polyphase metamorphism in metapelites from Sidironero complex (Rhodope domain, NE Greece). *Proc. XIX CBGA Congress, Thessaloniki* **100**, 173–181 (2010).
32. P. W. O. Hoskin, U. Schaltegger, The composition of zircon and igneous and metamorphic petrogenesis. *Rev. Mineral. Geochem.* **53**, 27–62 (2003).
33. D. Rubatto, Zircon trace element geochemistry: Partitioning with garnet and the link between U–Pb ages and metamorphism. *Chem. Geol.* **184**, 123–138 (2002).
34. K. R. Ludwig, User's manual for Isoplot 3.75: A geochronological toolkit for Microsoft Excel. *Berkeley Geochronology Center Spec. Pub.* **5**, 1–75 (2012).
35. D. J. Cherniak, W. A. Lanford, F. J. Ryerson, Lead diffusion in apatite and zircon using ion implantation and Rutherford Backscattering techniques. *Geochim. Cosmochim. Acta* **55**, 1663–1673 (1991).
36. N. E. Timms, S. M. Reddy, D. Healy, A. A. Nemchin, M. L. Grange, R. T. Pidgeon, R. Hart, Resolution of impact-related microstructures in lunar zircon: A shock-deformation mechanism map. *Meteorit. Planet Sci.* **47**, 120–141 (2012).
37. M. L. Grange, R. T. Pidgeon, A. A. Nemchin, N. E. Timms, C. Meyer, Interpreting U–Pb data from primary and secondary features in lunar zircon. *Geochim. Cosmochim. Acta* **101**, 112–132 (2013).
38. L. A. Bursill, A. C. McLaren, Transmission electron microscope study of natural radiation damage in zircon ($ZrSiO_4$). *Phys. Status Solidi B* **13**, 331–343 (1966).
39. B. Burton, M. V. Speight, The coarsening and annihilation kinetics of dislocation loop. *Philos. Mag. A* **53**, 385–402 (1986).
40. D. Mordehai, E. Clouet, M. Fivel, M. Verdier, Annealing of dislocation loops in dislocation dynamics simulations. *IOP Conf. Ser. Mater. Sci. Eng.* **3**, 012001 (2009).

41. G. Perillat-Merceroz, P. Gergaud, P. Marotel, S. Brochen, P-H. Jouneau, G. Feuillet, Formation and annealing of dislocation loops induced by nitrogen implantation of ZnO. *J. Appl. Phys.* **109**, 023513 (2011).
42. P. W. O. Hoskin, P. D. Kinny, D. Wyborn, B. W. Chappell, Identifying accessory mineral saturation during differentiation in granitoid magmas: An integrated approach. *J. Petrol.* **41**, 1365–1396 (2000).
43. G. S. Was, *Fundamentals of Radiation Materials Science* (Springer Science & Business Media, Berlin, 2007).
44. K. Hoummada, G. Tellouche, I. Blum, A. Portavoce, M. Descoins, D. Mangelinck, Direct observation of Ni decorated dislocation loops within $As^{+}$-implanted silicon and arsenic clustering in Ni silicide contact. *Microelectron. Eng.* **107**, 184–189 (2013).
45. A. R. C. Kylander-Clark, B. R. Hacker, J. M. Cottle, Laser-ablation split-stream ICP petrochronology. *Chem. Geol.* **345**, 99–112 (2013).
46. M. Wiedenbeck, P. Allé, F. Corfu, W. L. Griffin, M. Meier, F. Oberli, A. Von Quadt, J. C. Roddick, W. Spiegel, Three natural zircon standards for U-Th-Pb, Lu-Hf, trace element and REE analyses. *Geostand. Geoanal. Res.* **19**, 1–23 (1995).
47. S. E. Jackson, N. J. Pearson, W. L. Griffin, E. A. Belousova, The application of laser ablation-inductively coupled plasma-mass spectrometry to in situ U–Pb zircon geochronology. *Chem. Geol.* **211**, 47–69 (2004).
48. J. Sláma J. Košler, D. J. Condon, J. L. Crowley, A. Gerdes, J. M. Hanchar, M. S. A. Horstwood, G. A. Morris, L. Nasdala, N. Norberg, U. Schaltegger, B. Schoene, M. N. Tubrett, M. J. Whitehouse, Plešovice zircon—A new natural reference material for U–Pb and Hf isotopic microanalysis. *Chem. Geol.* **249**, 1–35 (2008).
49. W. R. Dickinson, G. E. Gehrels, U–Pb ages of detrital zircons from Permian and Jurassic eolian sandstones of the Colorado Plateau, USA: Paleogeographic implications. *Sediment. Geol.* **163**, 29–66 (2003).
50. C. Paton, J. D. Woodhead, J. C. Hellstron, J. M. Hergt, A. Greig, R. Maas, Improved laser ablation U-Pb zircon geochronology through robust downhole fractionation correction. *Geochem. Geophys. Geosyst.* **11**, Q0AA06 (2010)
51. G. W. Fynn, W. Powell, *The Cutting and Polishing of Electro-optic Materials* (Adam Hilger, London, 1979).
52. K. Thompson, D. Lawrence, D. J. Larson, J. D. Olson, T. F. Kelly, B. Gorman, In situ site-specific specimen preparation for atom probe tomography. *Ultramicroscopy* **107**, 131–139 (2007).
53. D. R. Snoeyenbos, D. Reinhard, D. P. Olson, Atomic scale imaging of U, Th and radiogenic Pb in zircon. *Mineral. Mag.* **76**, 2388 (2012).
54. A. Pérez-Huerta, F. Laiginhas, D. A. Reinhard, T. J. Prosa, R. L. Martens, Atom probe tomography (APT) of carbonate minerals. *Micron* **80**, 83–89 (2016).
55. L. M. Gordon, L. Tran, D. Joester, Atom probe tomography of apatites and bone-type mineralized tissues. *ACS Nano* **6**, 10667–10675 (2012).
56. J. Weber, J. Barthel, F. Brandt, M. Klinkenberg, U. Breuer, M. Kruth, D. Bosbach, Nano-structural features of barite crystals observed by electron microscopy and atom probe tomography. *Chem. Geol.* **424**, 51–59 (2016).
57. T. F. Kelly, D. J. Larson, Atom probe tomography 2012. *Annu. Rev. Mater. Res.* **42**, 1–31 (2012).

**Acknowledgments:** We thank R. Coish and J. Smith for analytical assistance; J. W. Valley and E. B. Watson for thoughtful, thorough reviews; and K. Hodges for editorial handling. **Funding:** This research was funded in part by NSF MRI 1530963 and Bowdoin College Research Funds to E.M.P. and ARC CE11E0070 and SIEF RI13-01 to S.M.R. The Advanced Resource Characterisation Facility under the auspices of the National Resource Sciences Precinct—a collaboration between the Commonwealth Scientific and Industrial Research Organization, Curtin University, and the University of Western Australia—was supported by the Science and Industry Endowment Fund. **Author contributions:** E.M.P. and D.R.S. collected the samples that initiated the project. E.M.P., S.M.R., D.W.S., W.D.A.R., and D.F. collected and processed the atom probe data. D.W.S. performed postprocessing of atom probe data. E.M.P. and A.R.C.K.-C. collected the LASS data. E.M.P. and S.M.R. wrote most of the paper. All authors reviewed and approved this paper. **Competing interests:** The authors declare that they have no competing interests. **Data and materials availability:** All data needed to evaluate the conclusions in the paper are present in the paper and/or the Supplementary Materials. Additional data related to this paper may be requested from the authors.

Submitted 10 June 2016
Accepted 2 August 2016
Published 2 September 2016
10.1126/sciadv.1601318

**Citation:** E. M. Peterman, S. M. Reddy, D. W. Saxey, D. R. Snoeyenbos, W. D. A. Rickard, D. Fougerouse, A. R. C. Kylander-Clark, Nanogeochronology of discordant zircon measured by atom probe microscopy of Pb-enriched dislocation loops. *Sci. Adv.* **2**, e1601318 (2016).

ScienceAdvances

# Nanogeochronology of discordant zircon measured by atom probe microscopy of Pb-enriched dislocation loops

Emily M. Peterman, Steven M. Reddy, David W. Saxey, David R. Snoeyenbos, William D. A. Rickard, Denis Fougerouse and Andrew R. C. Kylander-Clark

*Sci Adv* **2** (9), e1601318.
DOI: 10.1126/sciadv.1601318